Parameter Identification and Adaptive Control of a High Power Medium Voltage Dual Active Bridge

1st Tobias Merz
Elektrotechnisches Institut (ETI)
Karlsruhe Institute of Technology (KIT)
Karlsruhe, Germany
tobias.merz@kit.edu

2nd Nikolas Menger
Elektrotechnisches Institut (ETI)
Karlsruhe Institute of Technology (KIT)
Karlsruhe, Germany

3rd Georg Zieglmaier
Elektrotechnisches Institut (ETI)
Karlsruhe Institute of Technology (KIT)
Karlsruhe, Germany

4th Fabian Sommer
Elektrotechnisches Institut (ETI)
Karlsruhe Institute of Technology (KIT)
Karlsruhe, Germany

5th Rüdiger Schwendemann
Elektrotechnisches Institut (ETI)
Karlsruhe Institute of Technology (KIT)
Karlsruhe, Germany

6th Marc Hiller
Elektrotechnisches Institut (ETI)
Karlsruhe Institute of Technology (KIT)
Karlsruhe, Germany

***Abstract*—A unified control software is typically designed and tuned for structurally identical Dual Active Bridges (DABs) based on worst-case hardware parameters. However, improving dynamic behavior, efficiency and resource utilization requires precise knowledge of each individual unit, since even identically built systems may exhibit different characteristics due to component tolerances and varying operating conditions. This necessitates either additional sensors or individual testing and adaptation of each DAB's control algorithm. To address this limitation, this work presents an online parameter identification method that estimates the leakage inductance with less than 2% deviation without requiring extra sensors. Additionally, the identified inductance is used to adjust the control algorithm in real time, thereby improving efficiency and enabling higher maximum output power by relaxing conservative software constraints, while ensuring operation within the safe operating area.**

***Index Terms*—DC-DC power converters, Dual Active Bridge, Parameter identification, Hardware utilization, Safe Operating Area**

I. Introduction

The Dual Active Bridge (DAB) is a promising galvanically isolated DC-DC converter topology suitable for a wide range of applications. As demonstrated in [1], for instance, future systems are expected to be produced in high volumes to leverage economies of scale and reduce costs. However, large-scale manufacturing introduces tolerances that lead to parameter variations between production batches. In addition, operating conditions such as temperature fluctuations and aging further influence the parameters of the DAB over time.

The control of power transfer in a DAB directly depends on the combined leakage inductance of the Medium-frequency transformer (MFT) and its connections to the semiconductors. To deal with these variations, which can reach up to $\pm 20\,\%$ [2], [3], while keeping development costs and complexity low, a standardized control system is typically applied across all similar designed DABs. Since individual testing and adjustment of each module are impractical, the control algorithm must be capable of handling worst-case parameter deviations. This requirement leads to a conservative controller design that limits the utilization of the hardware's full potential.

To overcome these limitations, online parameter identification and adaptive control become essential for maintaining and optimizing system performance. A major challenge in identifying leakage inductance in high-power MV DABs is the small inductance value and its interaction with the parasitic capacitances of the semiconductors during commutation. Although online identification of leakage inductance in DABs has been widely studied, most existing approaches have been validated on low-power systems ($< 2\,\mathrm{kW}$), where parasitic effects are less significant. Several representative methods have been proposed: [4] employs a recursive least-squares method to estimate the equivalent local leakage inductance. In [2], an adaptive deadbeat controller is introduced to identify both the leakage inductance and the output capacitance. However, its capacitance estimation depends on the inductance mismatch. The authors of [5] propose a model predictive control approach in which the leakage inductance is continuously adapted, but this method relies on accurate knowledge of the output capacitance of the DAB and neglects commutation effects. A semi-online identification method is presented in [6], which iteratively refines parameters by comparing measured and simulated data, although only modeled parasitics can be identified. Overall, these methods primarily aim to improve voltage control dynamics rather than achieve comprehensive system optimization.

This paper focuses on identifying the leakage inductance and its influence on the operation of a $450\,\mathrm{kW}$ DAB. The key distinction in high-power DABs lies in the pronounced non-linearity of their power transfer characteristics, as demonstrated in [7]. Instead of relying on a locally linearized equivalent inductance, the algorithm identifies the actual physical leakage inductance. Accurate identification enables improved control dynamics, better selection of modulation strategies, and enhanced utilization of semiconductor devices while maintaining their Safe Operating Area (SoA). These improvements

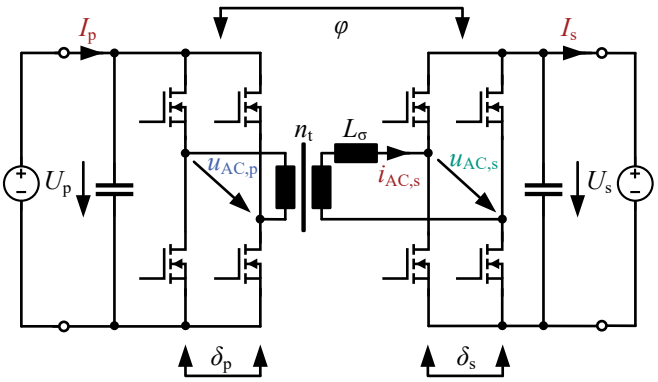

Fig. 1: Idealized equivalent circuit of DAB with constant voltage load.

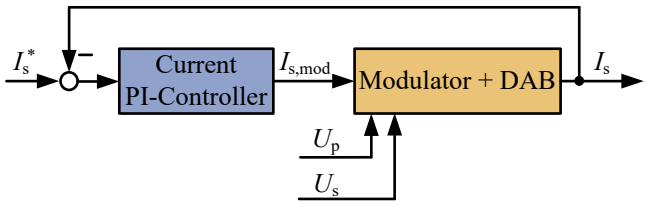

Fig. 2: Control structure of the DAB with PI-controller and modulator.

contribute to higher output power capability and increased reliability.

II. Topology and Modulation

Fig. 1 illustrates the ideal equivalent circuit of a DAB. The DC link voltages are denoted by U_x, and the corresponding AC voltages at the transformer terminals by $u_{\mathrm{AC},x}$, where $x \in \{\mathrm{p}, \mathrm{s}\}$ refers to the primary and secondary side of the DAB, respectively. The input and output currents are labeled as I_x, while the AC current on the transformer's secondary side is denoted by $i_{\mathrm{AC,s}}$. The transformer's leakage inductance is represented by L_σ, and its turn ratio by n_t. Fig. 2 shows the control structure of the DAB with the setpoint current I_s^*, the PI-controller and its output variable $I_{\mathrm{s,mod}}$.

A. SPS Modulation

While operating the DAB at unity gain voltage ratio ($n_\mathrm{t}U_\mathrm{p} \approx U_\mathrm{s}$) and high output power, Single Phase Shift (SPS) modulation is typically employed. When applying SPS modulation the power transfer characteristic of an ideal DAB can be described with (1), as first presented in [8]. The control variable φ represents the phase shift between the fundamental components of the AC voltages $u_{\mathrm{AC,p}}$ and $u_{\mathrm{AC,s}}$ generated by the two full-bridges. The variable f_sw represents the switching frequency of the DAB.

$$P_\mathrm{s}(\varphi) = U_\mathrm{s} \cdot I_\mathrm{s}(\varphi) = \frac{n_\mathrm{t} U_\mathrm{p} U_\mathrm{s}}{2\pi^2 f_\mathrm{sw} L_\sigma} \cdot \varphi(\pi - |\varphi|) \tag{1}$$

B. TCM Modulation

If the DAB is operated with lower power and buck ($n_\mathrm{t}U_\mathrm{p} > U_\mathrm{s}$) or boost ($n_\mathrm{t}U_\mathrm{p} < U_\mathrm{s}$) mode, typically Triangular Current Mode (TCM) modulation, as presented in [9], is applied. With TCM modulation three Degrees of Freedom (DoF), the phase shift φ between the full-bridges, and δ_p and δ_s as the phase shift within each full-bridge, are used to shape the current waveform in the AC path to a triangular shaped current. This ensures minimum RMS current and therefore minimal conduction losses [10]. The transmitted power is calculated with (2). The resulting additional phase shifts are then calculated as shown in (3) and (4).

$$P_{\mathrm{s,TCM}}(\varphi) = \\ = \operatorname{sign}(\varphi) \frac{\varphi^2 \cdot n_\mathrm{t} U_\mathrm{p} U_\mathrm{s}}{\pi^2 f_\mathrm{sw} L_\sigma \cdot |n_\mathrm{t}U_\mathrm{p} - U_\mathrm{s}|} \cdot \begin{cases} U_\mathrm{s} & \text{for } n_\mathrm{t}U_\mathrm{p} > U_\mathrm{s} \\ n_\mathrm{t}U_\mathrm{p} & \text{for } n_\mathrm{t}U_\mathrm{p} < U_\mathrm{s} \end{cases} \tag{2}$$

$$\delta_\mathrm{p} = \pi - \frac{U_\mathrm{s}}{|n_\mathrm{t}U_\mathrm{p} - U_\mathrm{s}|} \cdot 2 \cdot |\varphi| \tag{3}$$

$$\delta_\mathrm{s} = \pi - \frac{n_\mathrm{t}U_\mathrm{p}}{|n_\mathrm{t}U_\mathrm{p} - U_\mathrm{s}|} \cdot 2 \cdot |\varphi| \tag{4}$$

III. Proposed Algorithm

The online identification of the DAB's leakage inductance is based on comparing the idealized current transfer characteristic with actual operating behavior for positive and negative currents that exceed the threshold current $I_{\mathrm{s,ident,min}}$ during SPS modulation. This minimum identification current $I_{\mathrm{s,ident,min}}$ is calculated according to expected parasitic effects of the system such as the leakage inductance variations, commutation capacitances of the MOSFETs and non-linear control variables. These deviations between the ideal and the actual transfer characteristic provide information about the mismatch between the initially assumed and the actual leakage inductance. The implemented value of $L_{\sigma,\mathrm{sw}}$ is automatically updated accordingly, causing the controller, modulator, and operating limits to adjust to the new parameter. The overall identification process is illustrated in Fig. 3.

A. Mathematical derivation of the identification process

Equations (5) and (6) are both derived from the same idealized power transfer characteristic given in (1). The resulting output current I_s of a DAB can be calculated using (5), where all variables are representing the actual physical quantities of the converter. Additional parasitic effects, such as the commutation process, analyzed in [11], [12] and equivalent system resistances that affect the output current, are summarized in the error term ϵ.

$$I_\mathrm{s}(\varphi) = \frac{n_\mathrm{t}U_\mathrm{p}}{2\pi^2 f_\mathrm{sw} L_\sigma} \cdot \varphi(\pi - |\varphi|) + \epsilon \tag{5}$$

In contrast, (6) is used by the modulator to determine the phase shift angle φ from the modulator current setpoint $I_{\mathrm{s,mod}}$. The only difference between both equations is the value of the leakage inductance. While (5) uses the actual inductance L_σ, the modulator applies the software-defined value $L_{\sigma,\mathrm{sw}}$, which may deviate from the true physical value, i.e., $L_\sigma \neq L_{\sigma,\mathrm{sw}}$.

$$\varphi = \operatorname{sign}(I_{\mathrm{s,mod}}) \cdot \frac{\pi}{2} \left(1 - \sqrt{1 - \frac{8 f_\mathrm{sw} L_{\sigma,\mathrm{sw}} \cdot |I_{\mathrm{s,mod}}|}{n_\mathrm{t}U_\mathrm{p}}} \right) \tag{6}$$

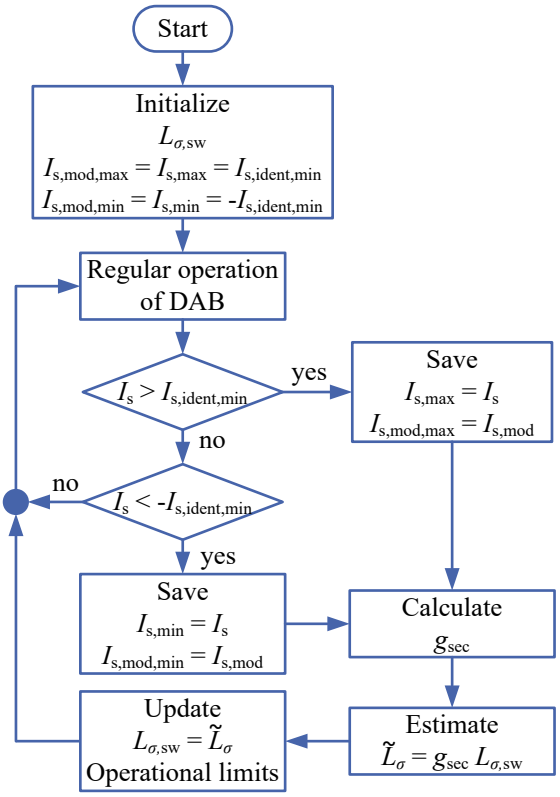

Fig. 3: Flowchart of the AC leakage inductance parameter identification.

As a result, the modulator current setpoint and the actual output current of the DAB differ, i.e., $I_\mathrm{s} \neq I_{\mathrm{s,mod}}$. This deviation can be used to derive a mathematical relationship. By applying the substitutions from (7) and (8), and inserting $\varphi(I_{\mathrm{s,mod}})$ from (6) into (5), the expression in (9) is obtained, assuming all other parameters are correctly defined.

$$A_{\mathrm{sub}} := \frac{n_\mathrm{t} U_\mathrm{p}}{2\pi^2 f_{\mathrm{sw}} L_\sigma} \cdot \mathrm{sign}(I_{\mathrm{s,mod}}) \tag{7}$$

$$B_{\mathrm{sub}} := 1 - \frac{8 f_{\mathrm{sw}} L_{\sigma,\mathrm{sw}} |I_{\mathrm{s,mod}}|}{n_\mathrm{t} U_\mathrm{p}}, \quad 0 \leq B_{\mathrm{sub}} \leq 1 \tag{8}$$

$$\begin{aligned} &I_\mathrm{s}(I_{\mathrm{s,mod}}) = \\ &= A_{\mathrm{sub}} \cdot \frac{\pi}{2}\left(1 - \sqrt{B_{\mathrm{sub}}}\right) \cdot \left[\pi - \left|\frac{\pi}{2}\left(1 - \sqrt{B_{\mathrm{sub}}}\right)\right|\right] + \epsilon \\ &= A_{\mathrm{sub}} \cdot \frac{\pi}{2}\left(1 - \sqrt{B_{\mathrm{sub}}}\right) \cdot \frac{\pi}{2}\left(1 + \sqrt{B_{\mathrm{sub}}}\right) + \epsilon \\ &= A_{\mathrm{sub}} \cdot \frac{\pi^2}{4}\left(1 - B_{\mathrm{sub}}\right) + \epsilon \\ &= \frac{n_\mathrm{t} U_\mathrm{p}}{2\pi^2 f_{\mathrm{sw}} L_\sigma} \cdot \mathrm{sign}(I_{\mathrm{s,mod}}) \cdot \frac{\pi^2}{4} \cdot \frac{8 f_{\mathrm{sw}} L_{\sigma,\mathrm{sw}} |I_{\mathrm{s,mod}}|}{n_\mathrm{t} U_\mathrm{p}} + \epsilon \\ &= \frac{L_{\sigma,\mathrm{sw}}}{L_\sigma} I_{\mathrm{s,mod}} + \epsilon \end{aligned} \tag{9}$$

Equation (9) shows that the output current I_s is proportional to the modulator setpoint $I_{\mathrm{s,mod}}$, scaled by the ratio of the implemented ($L_{\sigma,\mathrm{sw}}$) to the actual leakage inductance (L_σ), plus an error term ϵ. If the output current magnitude exceeds the threshold current $|I_\mathrm{s}| > I_{\mathrm{s,ident,min}}$, parasitic influences in the transfer function (TF) and therefore ϵ become negligible [7], [13]. With this assumption, the ratio g_{sec}, which represents the secant gradient of the TF for high-power operation points (OPs), can be calculated with (10). To identify the leakage inductance that best approximates the real value ($\tilde{L}_\sigma \approx L_\sigma$), (9) can be rearranged into (11).

$$g_{\mathrm{sec}} = \frac{I_{\mathrm{s,mod,max}} - I_{\mathrm{s,mod,min}}}{I_{\mathrm{s,max}} - I_{\mathrm{s,min}}} \tag{10}$$

$$L_\sigma \approx \tilde{L}_\sigma = g_{\mathrm{sec}} \cdot L_{\sigma,\mathrm{sw}} \tag{11}$$

The current pairs ($I_{\mathrm{s,mod,max}}$, $I_{\mathrm{s,max}}$) and ($I_{\mathrm{s,mod,min}}$, $I_{\mathrm{s,min}}$) required to evaluate (10) are tracked during regular operation at high-power OPs, either through an error storage system [13] or a superimposed value-tracking mechanism.

In typical implementations, a closed-loop controller, such as a PI-controller, continuously adjusts $I_{\mathrm{s,mod}}$ to minimize the deviation between the actual and the desired output current, i.e., $I_{\mathrm{s,mod}} \neq I_\mathrm{s} = I_\mathrm{s}^*$. The setpoint I_s^* is either defined by the application or actively modified to initiate an identification cycle. Although this superimposed controller affects $I_{\mathrm{s,mod}}$, it does not interfere with the inductance identification process, as the recorded current pairs remain valid.

B. Adaption of operation limits

As shown in (1) and (2), the maximum output power $P_{\mathrm{s,max}}$ of the DAB is directly influenced by the leakage inductance. When the maximum permissible AC peak current $\hat{i}_{\mathrm{AC}}$ is defined based on the switching current limits of the semiconductors, both the output power and the switching angle φ must be constrained according to the operating voltages and the expected leakage inductance. This is done according to (12) for SPS modulation and (13) for TCM modulation [14]. Consequently, accurately estimating the leakage inductance improves the precision of these limits. This either increases the maximum transmittable power and utilization if the leakage inductance is underestimated, or reduces the maximum output power if the leakage inductance is overestimated, ensuring operation within the SoA.

In operating regions where both modulation schemes are feasible, the choice between them and their respective limitations also affect power losses. Hence, the efficiency gain achieved through optimal modulation scheme selection depends directly on the accuracy of the identified leakage inductance.

$$P_{\mathrm{SPS,AC,max}} = \frac{n_\mathrm{t} U_\mathrm{p} U_\mathrm{s}}{8 f_{\mathrm{sw}} L_\sigma} \cdot \begin{cases} 1 - \left(\frac{n_\mathrm{t} U_\mathrm{p} - 4 f_{\mathrm{sw}} L_\sigma \cdot \hat{i}_{\mathrm{AC}}}{U_\mathrm{s}}\right)^2 & \text{for } n_\mathrm{t} U_\mathrm{p} \geq U_\mathrm{s} \\ 1 - \left(\frac{U_\mathrm{s} - 4 f_{\mathrm{sw}} L_\sigma \cdot \hat{i}_{\mathrm{AC}}}{n_\mathrm{t} U_\mathrm{p}}\right)^2 & \text{for } n_\mathrm{t} U_\mathrm{p} < U_\mathrm{s} \end{cases} \tag{12}$$

$$P_{\mathrm{TCM,AC,max}} = \frac{f_{\mathrm{sw}} L_\sigma \hat{i}_{\mathrm{AC}}^2}{|n_\mathrm{t} U_\mathrm{p} - U_\mathrm{s}|} \cdot \begin{cases} n_\mathrm{t} U_\mathrm{p} & \text{for } n_\mathrm{t} U_\mathrm{p} > U_\mathrm{s} \\ U_\mathrm{s} & \text{for } n_\mathrm{t} U_\mathrm{p} < U_\mathrm{s} \end{cases} \tag{13}$$

Fig. 4 illustrates the absolute increase in software limited maximum output power when ensuring SoA-compliant operation according to [14]. It shows the achievable power

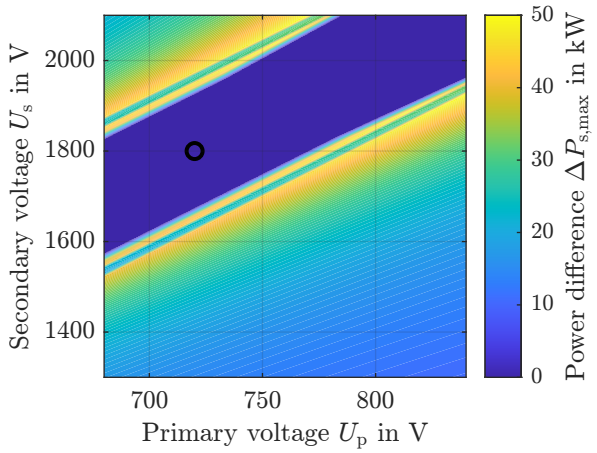

Fig. 4: Absolute increase $\Delta P_{\mathrm{s,max}} = P_{\mathrm{s,max}}(10.0\,\mu\mathrm{H}) - P_{\mathrm{s,max}}(9.0\,\mu\mathrm{H})$ in software limited maximum possible output power, if the actual leakage inductance L_σ is 10.0 µH instead of an expected $L_{\sigma,\mathrm{sw}} = 9.0\,\mu\mathrm{H}$. The black circle marks the nominal OP.

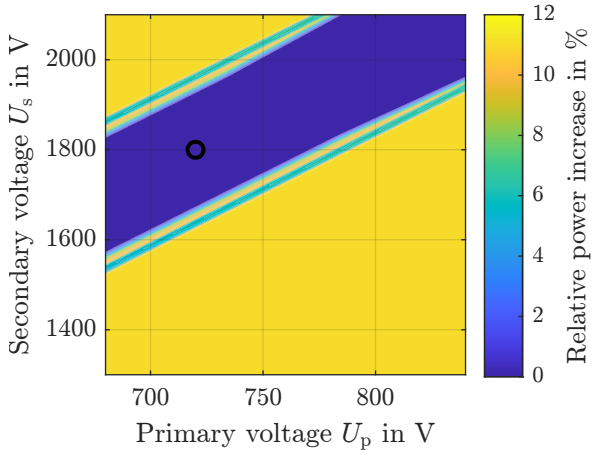

Fig. 5: Relative increase $\frac{\Delta P_{\mathrm{s,max}}}{P_{\mathrm{s,max}}}$ in software limited maximum possible output power, if the actual leakage inductance L_σ is 10.0 µH instead of an expected $L_{\sigma,\mathrm{sw}} = 9.0\,\mu\mathrm{H}$ ($\approx +11.1\,\%$). The black circle marks the nominal OP.

difference $\Delta P_{\mathrm{s,max}} = P_{\mathrm{s,max}}(10.0\,\mu\mathrm{H}) - P_{\mathrm{s,max}}(9.0\,\mu\mathrm{H})$ for the DAB described in Section IV, when the actual leakage inductance is $L_\sigma = 10.0\,\mu\mathrm{H}$ and the deviation from the initially assumed value of $L_{\sigma,\mathrm{sw}} = 9.0\,\mu\mathrm{H}$ is correctly identified. The corresponding relative increase is presented in Fig. 5. The black circle in both figures marks the nominal OP. When the DAB operates with a voltage gain close to unity, thus using SPS modulation, no improvement in maximum output power is achieved, since the power is then limited not by the leakage inductance but by maximum power losses. Conversely, if the actual leakage inductance is smaller than expected, the maximum output power must be reduced accordingly to maintain safe operation.

IV. System Setup

Fig. 6 illustrates the test bench configured as a back-to-back (B2B) setup consisting of two DABs to test the proposed method. Each DAB includes the complete power stage as well as the associated measurement and control electronics. One DAB controls the LV-side U_p, while the other serves as the device under test, in which the parameter identification and controller adaption are implemented. This DAB controls the output current I_s on the MV side and thus determines the transmitted output power P_s. The voltage on the secondary side is maintained by an external MV power supply.

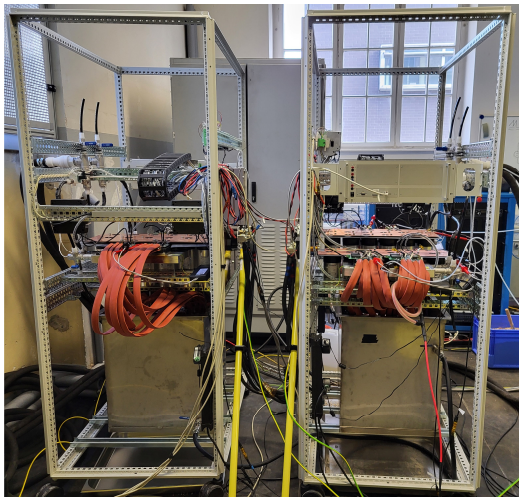

Fig. 6: Two 450 kW DABs configured in a B2B setup.

TABLE I
Parameters of the MV DAB referred to the secondary side

Parameter	Symbol	Value
Nominal output power	P_nom	450 kW
Primary voltage	U_p	680 V-840 V
Secondary voltage	U_s	1300 V-2100 V
Maximum output current	$\hat{I}_\mathrm{s}$	±250 A
Maximum AC current	$\hat{i}_\mathrm{AC}$	450 A
DAB switching and control frequency	$f_\mathrm{sw}, f_\mathrm{con}$	15 kHz
Semiconductors primary side	FMF1200DXZ-24B	
Semiconductors secondary side	FMF750DC-66A	
Transformer winding ratio	n_t	1 : 2.5
Leakage inductance	L_σ	9.0 µH
Magnetizing inductance	L_h	3.75 mH

The leakage inductance of the AC path, including the MFT and the connection cables, is approximately $L_\sigma \approx 9.0\,\mu\mathrm{H}$, and the magnetizing inductance is $L_\mathrm{h} \approx 3.75\,\mathrm{mH}$. Both values were measured using a Power Choke Tester DPG10-1000B. The relevant DAB parameters are summarized in Table I.

V. Experimental Results

This chapter presents the results of the identification process and the subsequent adaptation of the DAB. The physical leakage inductance is assumed to be $L_\sigma = 9.0\,\mu\mathrm{H}$ and remains constant throughout the tests. The minimum identification current of $I_{\mathrm{s,ident,min}} = 175\,\mathrm{A}$ is calculated according to datasheet values of the parasitic capacitances of the used semiconductors [15], [16].

A. Detecting the Leakage Inductance

Fig. 7 shows the resulting transfer characteristics for positive and negative currents. It can be seen that they approach a

TABLE II
Data tuples collected during the operation of the DAB with $U_\mathrm{p} = 720\,\mathrm{V}$ and modified values of $L_{\sigma,\mathrm{sw}}$ and U_s.
*: Measurement was conducted with $I_{\mathrm{s,max}} = 200\,\mathrm{A}$.

U_s	$L_{\sigma,\mathrm{sw}}$	$I_{\mathrm{s,mod,max}}$	$I_{\mathrm{s,mod,min}}$	$\tilde{L}_\sigma$
1800 V	7.0 µH	288.5 A*	−249.3 A	8.86 µH
1800 V	8.0 µH	283.2 A	−218.2 A	8.91 µH
1800 V	9.0 µH	251.1 A	−190.9 A	8.84 µH
1800 V	10.0 µH	226.8 A	−174.6 A	8.92 µH
1800 V	11.0 µH	205.5 A	−157.9 A	8.88 µH
1764 V	9.0 µH	231.5 A	−215.5 A	8.94 µH
1782 V	9.0 µH	244.7 A	−201.2 A	8.92 µH
1818 V	9.0 µH	261.5 A	−183.5 A	8.90 µH
1836 V	9.0 µH	268.5 A	−175.3 A	8.88 µH

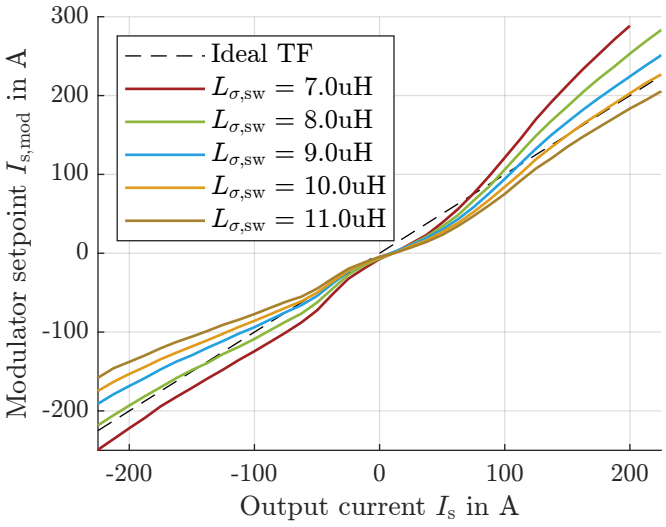

Fig. 7: Relationship between necessary modulator setpoint $I_{\mathrm{s,mod}}$ and output current I_s of the investigated DAB with $U_\mathrm{p} = 720\,\mathrm{V}$, $U_\mathrm{s} = 1800\,\mathrm{V}$ and different software-implemented leakage inductances $L_{\sigma,\mathrm{sw}}$.

constant gain for higher output currents I_s. The collected data tuples for high positive and negative output currents under SPS modulation are summarized in Table II. To evaluate the reliability of the detection process, both the secondary-side DC link voltage U_s and the implemented leakage inductance $L_{\sigma,\mathrm{sw}}$ were varied.

All data tuples for positive currents were recorded at $I_{\mathrm{s,max}} = 225\,\mathrm{A}$, except for the case with $L_{\sigma,\mathrm{sw}} = 7.0\,\mu\mathrm{H}$, where the current had to be limited to $I_{\mathrm{s,max}} = 200\,\mathrm{A}$ due to data-type issues. For negative currents, the output current was controlled to $I_{\mathrm{s,min}} = -225\,\mathrm{A}$. Substituting these tuples into (11) yields the identified leakage inductance $\tilde{L}_\sigma$, as shown in the last column. The deviation between the identified and measured inductances remains below 2 %, confirming the accuracy of the proposed algorithm. In fact, it can even be assumed that the actual leakage inductance in the operational setup is $8.9\,\mu\mathrm{H}$ rather than $9.0\,\mu\mathrm{H}$, as measured in the slightly modified test configuration.

B. Adaption of the modulation scheme

The measured efficiency gain in the boundary area between TCM and SPS is depicted in Fig. 8. The solid line, calculated with the actual leakage inductance of $L_\sigma = 9.0\,\mu\mathrm{H}$, represents

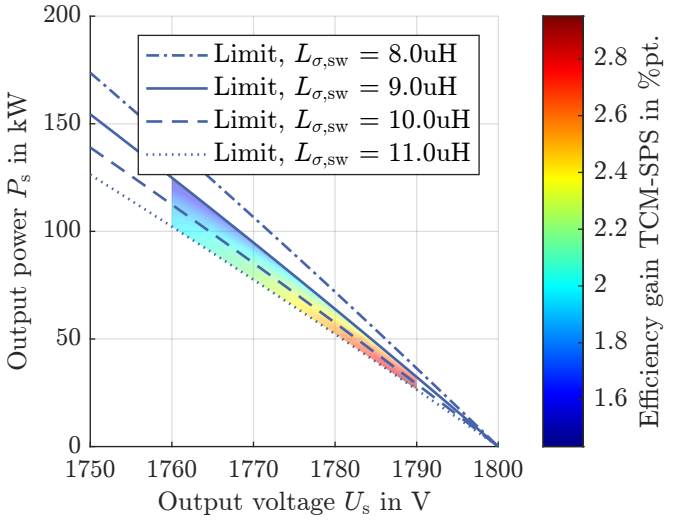

Fig. 8: Measured efficiency gain in %pt. in the boundary area, if TCM is used instead of SPS. The primary side voltage is set to $U_\mathrm{p} = 720\,\mathrm{V}$.

the physical limit of the output power for the given DAB with TCM. Above this limit, TCM modulation becomes unusable due to modulation constraints and must be replaced by another scheme, e.g. SPS. Below the solid line, both modulation schemes are applicable. However, in this operation area TCM consistently outperforms SPS in terms of efficiency. The dash-dotted, dashed and dotted lines correspond to calculated TCM power limits for leakage inductances of $8.0\,\mu\mathrm{H}$, $10.0\,\mu\mathrm{H}$ and $11.0\,\mu\mathrm{H}$, respectively.

Fig. 8 shows that if the leakage inductance is estimated to be bigger than the actual value, the controller reaches its calculated power limit earlier and prematurely switches to the less efficient SPS modulation. Therefore, accurate leakage inductance identification allows selecting the optimal modulation scheme in this boundary area, thereby improving efficiency by approximately 2%pt. In contrast, underestimating the leakage inductance has no significant impact, as the modulation scheme automatically changes from TCM to SPS when the physical output power limit is reached.

C. Update of the Power Limits

To illustrate the impact of deviations between the expected and actual leakage inductance on the achievable output power, the DAB is operated at its controller limits using TCM at $U_\mathrm{s} \approx 1440\,\mathrm{V}$. The maximum power at this OP is determined by the permissible transformer peak current $\hat{i}_\mathrm{AC}$.

Fig. 9 shows the resulting AC current $i_{\mathrm{AC,s}}$ in the time-domain during the positive current interval of the switching period. For these measurements, the maximum allowable AC current is set to $\hat{i}_\mathrm{AC} = 300\,\mathrm{A}$, indicated by the red area.

Due to the limited performance of the secondary-side power source, the voltage is not perfectly controlled to $U_\mathrm{s} = 1400\,\mathrm{V}$, but is superimposed by a ripple for the different OPs. Consequently, the slopes of the AC currents differ slightly. Nevertheless, the controller considers the measured instantaneous voltages and calculates the operational limitations accordingly.

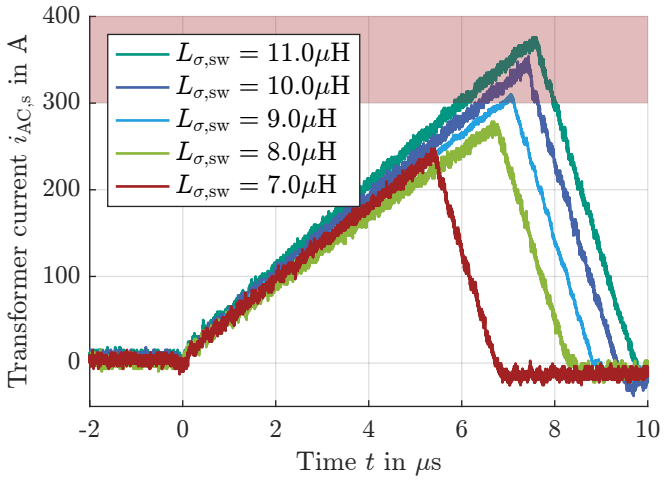

Fig. 9: Measured transformer currents $i_{\mathrm{AC,s}}$ with a maximum permissible AC current $\hat{i}_{\mathrm{AC,max}} = 300\,\mathrm{A}$. Operation with TCM and $U_{\mathrm{s}} = 1440\,\mathrm{V}$.

If the expected leakage inductance is higher than the actual inductance (dark green and dark blue lines), the AC peak current exceeds the specified SoA of the system, reaching up to $i_{\mathrm{AC,s}} = 350\,\mathrm{A}$ in this example. Conversely, if the expected inductance is lower than the actual value (light green and red lines), the controller prematurely limits the output power, resulting in underutilization of the system. When the leakage inductance is correctly identified and the expected value is updated accordingly (light blue line), the AC peak current remains within approximately $\pm 5\,\%$ of the specified transformer peak current $\hat{i}_{\mathrm{AC}}$. This ensures operation within the SoA while increasing hardware utilization.

VI. Conclusion

This paper presents an online methodology for identifying the combined leakage inductance of the MFT and its connection wires, and for automatically updating the corresponding software parameter in a DAB. The method compares the modulator current setpoints with the measured secondary currents and applies a secant-gradient evaluation of the transfer characteristic to estimate the deviation between the implemented and the actual leakage inductance. Experimental validation demonstrates that the identified inductance deviates by less than $2\,\%$ from reference measurements obtained with specialized laboratory equipment.

Incorporating the accurately identified inductance into the control and observer algorithm originally designed for worst-case conditions enables improved control and more precise estimation of transformer peak current. This ensures operating in the SoA of the semiconductors, while improving hardware utilization of the system. Moreover, precise parameter estimation supports a better evaluation of modulation boundaries resulting in an improved efficiency by up to $2\,\%$pt. at specific operating points.

Acknowledgment

The authors gratefully acknowledge funding by the German Federal Ministry of Research, Technology and Space (BMFTR) within the Kopernikus Project ENSURE ‘New ENergy grid StructURes for the German Energiewende’.

References

[1] M. Ichinose, K. Gorai, H. Miyata, R. Gomi, and K. Furukawa, “Transition to Carbon Neutrality in the EV Value Chain Multi-port EV Charger Contributes to Effective Energy Use Solutions in an EV Society,” Tech. Rep. June, 2024.

[2] T. Q. Duong and S. J. Choi, “Deadbeat Control With Bivariate Online Parameter Identification for SPS-Modulated DAB Converters,” *IEEE Access*, vol. 10, pp. 54 079–54 090, 2022.

[3] A. Campos, P. Dworakowski, B. Asllani, and K. Vershinin, “Influence of the Mission Profile on the Selection of the Leakage Inductance for DAB converter Keywords Case study and specifications,” *EPE*, 2025.

[4] Z. Guo, Y. Luo, and K. Sun, “Parameter Identification of the Series Inductance in DAB Converters,” *IEEE Transactions on Power Electronics*, vol. 36, no. 7, pp. 7395–7399, 2021.

[5] Y. Zhu, Y. Yang, H. Wen, J. Mao, P. Wang, X. Fan, W. Huang, Z. Zhao, S. Mekhilef, and J. Rodriguez, “Model Predictive Control with a Novel Parameter Identification Scheme for Dual-Active-Bridge Converters,” *IEEE Journal of Emerging and Selected Topics in Power Electronics*, vol. 11, no. 5, pp. 4704–4713, 2023.

[6] Q. Shang, F. Xiao, Y. Fan, H. Qing, and R. Wang, “A Non-Invasive Method for Parametric Identification of Dual-Active-Bridge Converter,” *2023 IEEE International Conference on Sensors, Electronics and Computer Engineering, ICSECE 2023*, pp. 1679–1683, 2023.

[7] F. Sommer, T. Merz, H. Sui, R. Schwendemann, and M. Hiller, “Analysis and Compensation of the ZVS based Nonlinear Transfer Characteristic of a Dual Active Bridge,” *2024 IEEE 10th International Power Electronics and Motion Control Conference, IPEMC 2024 ECCE Asia*, pp. 1169–1175, 2024.

[8] R. W. A. A. D. Doncker, D. M. Divan, and M. H. Kheraluwala, “A Three-Phase Soft-Switched High-Power-Density dc/dc Converter for High-Power Applications,” *IEEE TRANSACTIONS ON INDUSTRY APPLICATIONS, VOL. 27, NO. 1, JANUARYIFEBRUARY 1991 A*, vol. 27, no. 1, p. 11, 1991.

[9] N. Schibli, “Symmetrical Multilevel Converters with two Quadrant DC-DC Feeding,” Ph.D. dissertation, EPFL, 2000.

[10] F. Krismer and J. W. Kolar, “Closed form solution for minimum conduction loss modulation of DAB converters,” *IEEE Transactions on Power Electronics*, vol. 27, no. 1, pp. 174–188, 2012.

[11] B. Zhao, Q. Song, W. Liu, and Y. Sun, “Dead-time effect of the high-frequency isolated bidirectional full-bridge DC-DC converter: Comprehensive theoretical analysis and experimental verification,” *IEEE Transactions on Power Electronics*, vol. 29, no. 4, pp. 1667–1680, 2014.

[12] F. Sommer, N. Menger, T. Merz, N. Soltau, S. Idaka, and M. Hiller, “Time Domain Modeling of Zero Voltage Switching behavior considering Parasitic Capacitances for a Dual Active Bridge,” *ICPE 2023-ECCE Asia - 11th International Conference on Power Electronics - ECCE Asia: Green World with Power Electronics*, vol. 2, pp. 13–20, 2023.

[13] T. Merz, F. Sommer, R. Schwendemann, H. Sui, and M. Hiller, “Error Storage Based Online Linearization of the Nonlinear Transfer Function of a High Power Dual Active Bridge,” *2024 IEEE 10th International Power Electronics and Motion Control Conference, IPEMC 2024 ECCE Asia*, pp. 226–232, 2024.

[14] G. Zieglmaier, F. Sommer, T. Merz, and M. Hiller, “Highly Dynamic Voltage Control of a Dual Active Bridge over the Full Voltage Range by Operating Point Dependent Manipulated Variable Limitation,” in *PCIM Europe 2022; International Exhibition and Conference for Power Electronics, Intelligent Motion, Renewable Energy and Energy Management*, vol. 2023-May. VDE, 2023.

[15] MITSUBISHI ELECTRIC CORPORATION, “Datasheet FMF750DC-66A,” pp. 1–8, 2019.

[16] ——, “Datasheet FMF1200DXZ-24B,” pp. 1–13, 2022.